

# Analysis and optimization on the angular color shift of RGB OLED displays

GUANJUN TAN,<sup>1</sup> JIUN-HAW LEE,<sup>2</sup> SHENG-CHIEH LIN,<sup>2</sup> RUIDONG ZHU,<sup>1</sup>  
SANG-HUN CHOI,<sup>1</sup> AND SHIN-TSON WU<sup>1,\*</sup>

<sup>1</sup>College of Optics and Photonics, University of Central Florida, Orlando, FL 32816, USA

<sup>2</sup>Graduate Institute of Photonics and Optoelectronics and Department of Electrical Engineering,  
National Taiwan University, Taiwan

\*swu@creol.ucf.edu

**Abstract:** Microcavities contribute to enhancing the optical efficiency and color saturation of an organic light emitting diode (OLED) display. A major tradeoff of the strong cavity effect is its apparent color shift, especially for RGB-based OLED displays, due to their mismatched angular intensity distributions. To mitigate the color shift, in this work we first analyze the emission spectrum shifts and angular distributions for the OLEDs with strong and weak cavities, both theoretically and experimentally. Excellent agreement between simulation and measurement is obtained. Next, we propose a systematic approach for RGB-OLED displays based on multi-objective optimization algorithms. Three objectives, namely external quantum efficiency (EQE), color gamut coverage, and angular color shift of primary and mixed colors, can be optimized simultaneously. Our optimization algorithm is proven to be effective for suppressing color shift while keeping a relatively high optical efficiency and wide color gamut.

© 2017 Optical Society of America under the terms of the [OSA Open Access Publishing Agreement](#)

**OCIS codes:** (140.3948) Microcavity devices; (160.4890) Organic materials; (230.3670) Light-emitting diodes; (330.1690) Color.

## References and links

1. C. W. Tang and S. A. Vanslyke, "Organic electroluminescent diodes," *Appl. Phys. Lett.* **51**(12), 913–915 (1987).
2. K. T. Kamtekar, A. P. Monkman, and M. R. Bryce, "Recent advances in white organic light-emitting materials and devices (WOLEDs)," *Adv. Mater.* **22**(5), 572–582 (2010).
3. C.-H. Hsiao, Y.-H. Lan, P.-Y. Lee, T.-L. Chiu, and J.-H. Lee, "White organic light-emitting devices with ultra-high color stability over wide luminance range," *Org. Electron.* **12**(3), 547–555 (2011).
4. F. So, J. Kido, and P. Burrows, "Organic light-emitting devices for solid-state lighting," *MRS Bull.* **33**(7), 663–669 (2008).
5. F. Peng, H. Chen, F. Gou, Y. H. Lee, M. Wand, M. C. Li, S. L. Lee, and S. T. Wu, "Analytical equation for the motion picture response time of display devices," *J. Appl. Phys.* **121**(2), 023108 (2017).
6. H. Chen, J.-H. Lee, B.-Y. Lin, S. Chen, and S. T. Wu, "Liquid crystal display and organic light-emitting diode display: Present status and future perspectives," *Light Sci. Appl.* **7**, e17168 (2018), doi:10.1038/lsa.2017.168.
7. T. Tsujimura, *OLED Display Fundamentals and Applications* (John Wiley & Sons, 2012).
8. M. H. Lu, M. S. Weaver, T. X. Zhou, M. Rothman, R. C. Kwong, M. Hack, and J. J. Brown, "High-efficiency top-emitting organic light-emitting devices," *Appl. Phys. Lett.* **81**(21), 3921–3923 (2002).
9. L. H. Smith, J. A. E. Wasey, and W. L. Barnes, "The light out-coupling efficiency of top emitting organic light-emitting diodes," *Appl. Phys. Lett.* **84**(16), 2986–2988 (2004).
10. E. Kim, J. Chung, J. Lee, H. Cho, N. S. Cho, and S. Yoo, "A systematic approach to reducing angular color shift in cavity-based organic light-emitting diodes," *Org. Electron.* **48**, 348–356 (2017).
11. Q. Wang, Z. Deng, and D. Ma, "Realization of high efficiency microcavity top-emitting organic light-emitting diodes with highly saturated colors and negligible angular dependence," *Appl. Phys. Lett.* **94**(23), 233306 (2009).
12. D.-S. Leem, S.-Y. Kim, J.-H. Lee, and J.-J. Kim, "High efficiency p-i-n top-emitting organic light-emitting diodes with a nearly Lambertian emission pattern," *J. Appl. Phys.* **106**(6), 063114 (2009).
13. M.-K. Wei, J.-H. Lee, H.-Y. Lin, Y.-H. Ho, K.-Y. Chen, C.-C. Lin, C.-F. Wu, H.-Y. Lin, J.-H. Tsai, and T.-C. Wu, "Efficiency improvement and spectral shift of an organic light-emitting device by attaching a hexagon-based microlens array," *J. Opt. A, Pure Appl. Opt.* **10**(5), 055302 (2008).
14. M. Thomschke, R. Nitsche, M. Furno, and K. Leo, "Optimized efficiency and angular emission characteristics of white top-emitting organic electroluminescent diodes," *Appl. Phys. Lett.* **94**(8), 083303 (2009).
15. P. Yeh, *Optical Waves in Layered Media* (John Wiley & Sons, 1988).

16. K. A. Neyts, "Simulation of light emission from thin-film microcavities," *J. Opt. Soc. Am. A* **15**(4), 962–971 (1998).
17. R. Zhu, Z. Luo, and S.-T. Wu, "Light extraction analysis and enhancement in a quantum dot light emitting diode," *Opt. Express* **22**(S7), A1783–A1798 (2014).
18. G. Tan, R. Zhu, Y.-S. Tsai, K.-C. Lee, Z. Luo, Y.-Z. Lee, and S.-T. Wu, "High ambient contrast ratio OLED and QLED without a circular polarizer," *J. Phys. D Appl. Phys.* **49**(31), 315101 (2016).
19. W. Brütting, J. Frischeisen, T. D. Schmidt, B. J. Scholz, and C. Mayr, "Device efficiency of organic light-emitting diodes: progress by improved light outcoupling," *Phys. Status Solidi* **210**(1), 44–65 (2013).
20. S. Hofmann, M. Thomschke, B. Lüssem, and K. Leo, "Top-emitting organic light-emitting diodes," *Opt. Express* **19**(S6), A1250–A1264 (2011).
21. M. Born and E. Wolf, *Principles of Optics*, 7th (expanded) ed. (Cambridge University, Cambridge, 1999).
22. R. Hunt, *Measuring Colour*, 4th ed. (John Wiley & Sons, 2011).
23. M. D. Fairchild, *Color Appearance Models*, 3rd ed. (Wiley, 2013).
24. S. Kim, H.-J. Kwon, S. Lee, H. Shim, Y. Chun, W. Choi, J. Kwack, D. Han, M. Song, S. Kim, S. Mohammadi, I. Kee, and S. Y. Lee, "Low-power flexible organic light-emitting diode display device," *Adv. Mater.* **23**(31), 3511–3516 (2011).
25. S.-F. Chen and C.-W. Wang, "Influence of the hole injection layer on the luminescent performance of organic light emitting diodes," *Appl. Phys. Lett.* **85**(5), 765–767 (2004).
26. J.-B. Kim, J.-H. Lee, C. K. Moon, S.-Y. Kim, and J.-J. Kim, "Highly enhanced light extraction from surface plasmonic loss minimized organic light-emitting diodes," *Adv. Mater.* **25**(26), 3571–3577 (2013).
27. D. Zhao, H. Liu, Y. Miao, H. Wang, B. Zhao, Y. Hao, F. Zhu, and B. Xu, "A red tandem organic light-emitting diode based on organic photovoltaic-type charge generation layer," *Org. Electron.* **32**, 1–6 (2016).
28. Z. Gao, F. Wang, K. Guo, H. Wang, B. Wei, and B. Xu, "Carrier transfer and luminescence characteristics of concentration-dependent phosphorescent Ir (ppy)<sub>3</sub> doped CBP film," *Opt. Laser Technol.* **56**, 20–24 (2014).
29. M. T. Lee, C. H. Liao, C. H. Tsai, and C. H. Chen, "Highly efficient, deep-blue doped organic light-emitting devices," *Adv. Mater.* **17**(20), 2493–2497 (2005).
30. B. W. D'Andrade and J. J. Brown, "Organic light-emitting device luminaire for illumination applications," *Appl. Phys. Lett.* **88**(19), 192908 (2006).
31. Y. Sakai, M. Shibata, and D. Yokoyama, "Simple model-free estimation of orientation order parameters of vacuum-deposited and spin-coated amorphous films used in organic light-emitting diodes," *Appl. Phys. Express* **8**(9), 096601 (2015).
32. H. Riel, S. Karg, T. Beirlein, W. Rieß, and K. Neyts, "Tuning the emission characteristics of top-emitting organic light-emitting devices by means of a dielectric capping layer: An experimental and theoretical study," *J. Appl. Phys.* **94**(8), 5290–5296 (2003).
33. L. S. Hung, C. W. Tang, M. G. Mason, P. Raychaudhuri, and J. Madathil, "Application of an ultrathin LiF/Al bilayer in organic surface-emitting diodes," *Appl. Phys. Lett.* **78**(4), 544–546 (2001).
34. H. Riel, S. Karg, T. Beirlein, B. Ruhstaller, and W. Rieß, "Phosphorescent top-emitting organic light-emitting devices with improved light outcoupling," *Appl. Phys. Lett.* **82**(3), 466–468 (2003).
35. A. B. Chwang, M. A. Rothman, S. Y. Mao, R. H. Hewitt, M. S. Weaver, J. A. Silvernail, K. Rajan, M. Hack, J. J. Brown, X. Chu, L. Moro, T. Krajewski, and N. Rutherford, "Thin film encapsulated flexible organic electroluminescent displays," *Appl. Phys. Lett.* **83**(3), 413–415 (2003).
36. A. P. Ghosh, L. J. Gerenser, C. M. Jarman, and J. E. Fornalik, "Thin-film encapsulation of organic light-emitting devices," *Appl. Phys. Lett.* **86**(22), 223503 (2005).
37. J.-S. Park, H. Chae, H. K. Chung, and S. I. Lee, "Thin film encapsulation for flexible AM-OLED: a review," *Semicond. Sci. Technol.* **26**(3), 034001 (2011).
38. H. Jung, H. Jeon, H. Choi, G. Ham, S. Shin, and H. Jeon, "Al<sub>2</sub>O<sub>3</sub> multi-density layer structure as a moisture permeation barrier deposited by radio frequency remote plasma atomic layer deposition," *J. Appl. Phys.* **115**(7), 073502 (2014).
39. F. B. Sun, Y. Duan, Y. Q. Yang, P. Chen, Y. H. Duan, X. Wang, D. Yang, and K. W. Xue, "Fabrication of tunable [Al<sub>2</sub>O<sub>3</sub>:Alucone] thin-film encapsulations for top-emitting organic light-emitting diodes with high performance optical and barrier properties," *Org. Electron.* **15**(10), 2546–2552 (2014).
40. C. H. Yang, P. Yin, J. H. Tao, J. C. Hsiao, M. T. Lee, H. H. Lu, and Y. H. Lin, "Novel thin film encapsulation structure for wearable plastic AMOLED display," *SID Symp. Dig. Tech. Papers* **47**, 841–843 (2016).
41. C. A. C. Coello and G. B. Lamont, *Applications of Multi-Objective Evolutionary Algorithms* (World Scientific, 2004).
42. C. S. McCamy, H. Marcus, and J. G. Davidson, "A color-rendition chart," *J. Appl. Photogr. Eng.* **2**(3), 95–99 (1976).

## 1. Introduction

Organic light emitting diode (OLED) is emerging as a promising technology for displays [1, 2] and general lighting [3, 4]. For display applications, OLED exhibits advantages in true black state, fast response time, color purity and flexibility [5, 6], in comparison with liquid crystal display (LCD). There are two main structural configurations, namely white OLED and

RGB OLED. In a white OLED display, red (R), green (G) and blue (B) emitter layers are stacked together to generate white pixels, and a patterned RGB color filter array is used to produce the desired colors. While in a RGB OLED display, individual red, green and blue sub-pixels are placed next to one another. Without the need of color filters, RGB OLED exhibits a lower power consumption and better color purity than white OLED. Active matrix OLED with RGB sub-pixels is gaining popularity for smartphone displays [7]. In order to improve optical efficiency and color purity, top-emitting OLED with two metallic electrodes utilizing strong microcavity resonance has been widely adopted [8, 9]. Although microcavity effect helps narrow the emission spectra, it causes color shift at large viewing angle. Due to Fabry–Perot resonance, the trade-offs between optical efficiency, color purity, and angular color shift inevitably exist. How to optimize the device performance becomes an urgent task.

As for the RGB OLED display system, color shifts actually originate from two factors [10]. The first one is directly related to the microcavity resonance. For each individual subpixel, its emission spectrum would shift toward a shorter wavelength as viewing angle increases, which is known as *blue shift* in an optical cavity. The angular color shifts of RGB primary colors can be clearly explained by blue shift. However, the primary colors usually only account for a small portion of the displayed images. The majority are those colors created by mixing RGB colors with different ratios. As to the mixed colors, there arises another non-negligible or even more critical factor. The mismatched angular emission distributions of RGB OLEDs can also result in angular color shift. For instance, if the angular distributions of red and blue subpixels decline faster than that of green, the white point of the display would look greenish at large viewing angle. Therefore, to analyze the color shift of a RGB OLED display, these two factors, namely microcavity resonance effect and angular distribution mismatch, need to be taken into consideration simultaneously. Some prior arts have discussed the angular color shift of monochrome OLEDs [11–14], where only the microcavity effect needs to be considered. Very few system-level investigation on the angular color shift of RGB OLED displays has been reported [10].

In this paper, we analyze the angular color shift of RGB OLED displays at system level, by considering both microcavity resonance shift and angular distribution mismatch. We first validate our proposed simulation model by experiment. In our experiment, two groups of OLED devices with strong and weak microcavity, respectively, are studied. Excellent agreement between simulation and measurement is achieved. Based on our model, we then develop a systematic optimization algorithm, which can simultaneously optimize external quantum efficiency (EQE), color gamut coverage, and angular color shift. With the help of the proposed systematic optimization, indistinguishable color shift can be achieved while keeping high EQE and wide color gamut.

## 2. Theory

In our analysis, we need to examine not only optical efficiency but also emission spectra at each viewing angles. Thus, we use the rigorous dipole model for planar OLED structure, which describes the emission characterization of isotropic emitter within a multilayer medium. The thin film multilayer can be first simplified to a three-layer structure by the transfer matrix approach [15] or iterative calculation [16]. The emitters in OLED emitting layer are modelled as randomly oriented dipoles. Both transverse magnetic (TM) and transverse electric (TE) waves need to be taken into consideration. The quantitative power dissipation density  $K$  of randomly oriented dipoles can be expressed by [16–18]:

$$K(k_x, \lambda) = \frac{1}{3}K_{TMv} + \frac{2}{3}(K_{TMh} + K_{TEh}), \quad (1)$$

where the subscripts  $v$  and  $h$  represent the vertical and horizontal dipoles, respectively, and  $k_x$  is the in-plane wave vector. The detailed description of each term in Eq. (1) can be found in [16, 17]. The power dissipation density  $K(k_x, \lambda)$  includes complete information of OLED

emission. We can then obtain optical efficiency, spectral and angular distributions from  $K(k_x, \lambda)$ .

Optical outcoupling efficiency of OLEDs can be evaluated by the dipole model [16]. The external quantum efficiency (EQE) is defined as [19]:

$$EQE = \eta \cdot IQE = \eta \cdot \gamma \cdot \eta_{S/T} \cdot q_{eff}, \quad (2)$$

where  $\eta$  is the outcoupling efficiency and  $IQE$  is the internal quantum efficiency, which is the product of effective quantum yield  $q_{eff}$ , charge carrier balance  $\gamma$ , and singlet/triplet capture ratio  $\eta_{S/T}$  [19, 20]. Since our major focus here is on the optical outcoupling efficiency, without losing generality let us assume the internal quantum efficiency is 100%. The optical modes are then extracted from power dissipation  $K$  by the in-plane wave vector  $k_x$  [17, 18]. Detailed descriptions of these modes are as follows: 1) direct emission (or air mode) with  $0 < k_x < k_0 \cdot n_{air}$  ( $k_0 = 2\pi/\lambda$  is the vacuum wave vector), indicating the light directly emitting into air; 2) substrate mode with  $k_0 \cdot n_{air} < k_x \leq k_0 \cdot n_{sub}$ , depicting the light trapped in substrate due to total internal reflection (TIR); 3) waveguide mode with  $k_0 \cdot n_{sub} < k_x \leq k_0 \cdot n_{eff}$ , showing the light guided inside the OLED layers, where  $n_{eff}$  is the equivalent refractive index [17, 18] of the organic layers and transparent electrode (the reflective metal electrode and the glass substrate are not included); and 4) surface plasmons mode with  $k_0 \cdot n_{eff} < k_x$ , corresponding to the evanescent wave at the organic/metal interface.

Equation (1) only gives the power dissipation at a single wavelength. To further evaluate the spectral and angular distributions, we take the photoluminescence (PL) spectra  $S(\lambda)$  as the weight ratio [17, 19]. In an OLED device, the substrate thickness is usually in the order of millimeter so that the optical interference effects play no role. Therefore, the substrate can be first assumed as a semi-infinite medium in our dipole model simulations. Next, the air-substrate interface can be calculated by Fresnel equations [21]. Once the respective spectral and angular distributions of RGB OLED emissions are obtained, we can calculate the CIE coordinates for the primary and mixed colors. Since the CIE coordinate value is actually quite sensitive to the spectrum profile, the accuracy of EL spectrum simulation becomes critical. Thus, the wavelength dispersion of refractive index of each layer must be considered as well. More detailed theoretical description and simulation process of OLED emission have been exhaustively discussed in previous publications [16–18]. All the simulations carried out in this work are based on our home-made MATLAB code. We also compared and verified this simulation model with commercial software packages, such as RSoft and FDTD solutions.

### 3. Experimental verification

Table 1. Layer structures of the six OLED samples we fabricated (Unit: nm).

Devices	Anode		HIL	HTL	EML	ETL	EIL	Cathode
	ITO	Al	MoO <sub>3</sub>	NPB	Alq <sub>3</sub>	BPhen	LiF	Al
1						40		
2	80	–	–	40	10	60	1	100
3						80		
4						40		
5	80	20	20	40	10	60	1	100
6						80		

In order to validate that our simulation model can be used to evaluate the color shift of OLED devices precisely, we carried out some experiments. We fabricated two groups of OLED devices with different strength of microcavity effect. The 3 strong-microcavity OLED

samples employ aluminum (Al) as both reflective cathode and semi-transparent anode. While for the weak microcavity group (also 3 samples), indium tin oxide (ITO) was adopted as the transparent anode. In all the six OLED samples we prepared, we used *N,N*-Bis (naphthalen-1-yl)-*N,N*-bis (phenyl) benzidine (NPB), 4,7-diphenyl-1,10-phenanthroline (BPhen), and LiF as hole transporting layer (HTL), electron transporting layer (ETL), and electron injection layer (EIL), respectively. Green emitting material tris-(8-hydroxyquinoline) aluminum ( $\text{Alq}_3$ ) was employed as the emissive layer (EML). As for the strong microcavity group,  $\text{MoO}_3$  was inserted between semi-transparent electrode and NPB as hole injection layer (HIL). Detailed layer structure of the OLED devices we fabricated are summarized in Table 1. The ETL thickness of both weak microcavity (devices 1~3) and strong microcavity (devices 4~6) OLEDs varies from 40 nm to 80 nm.

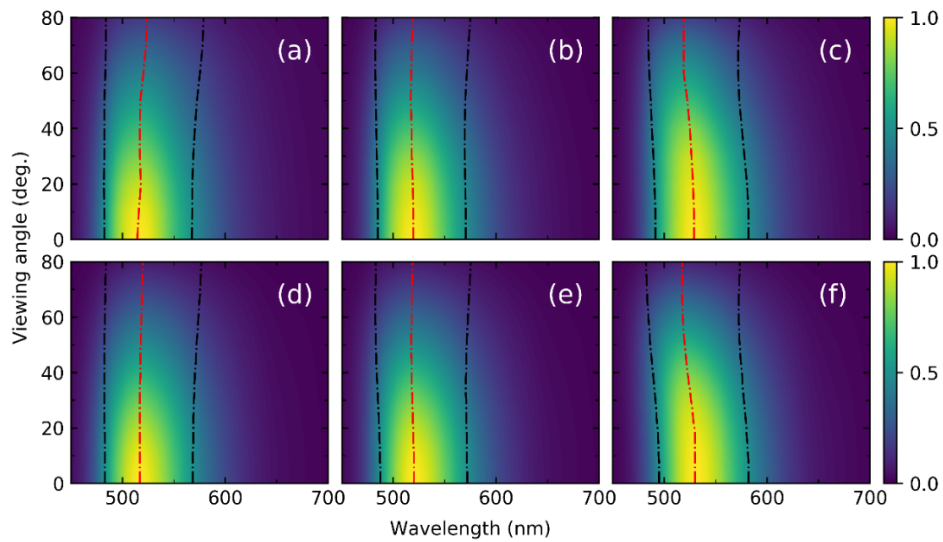


Fig. 1. EL spectra of weak cavity OLEDs at different viewing angles. Measured results: a) device 1; b) device 2 and c) device 3. Simulated results: d) device 1; e) device 2 and f) device 3.

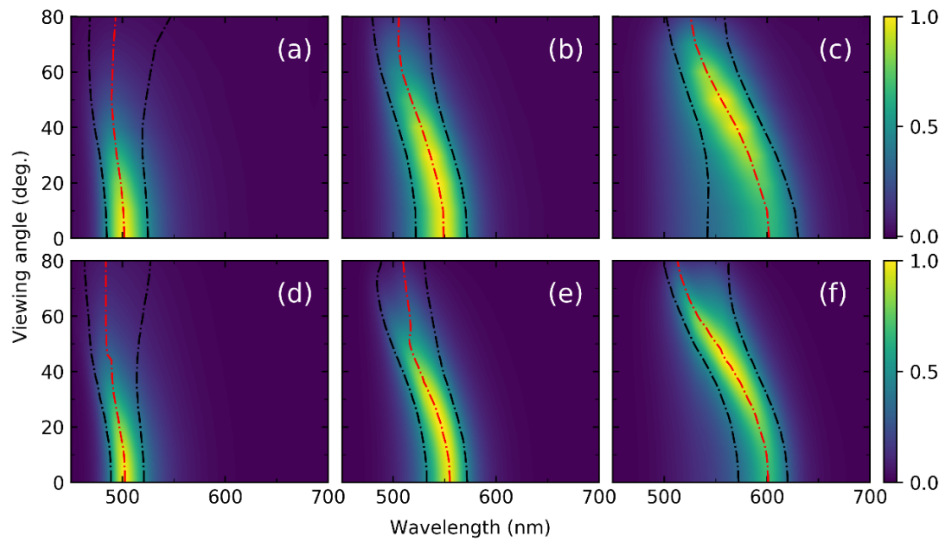


Fig. 2. EL spectra of strong cavity OLEDs at different viewing angles. Measured results: a) device 4; b) device 5, and c) device 6. Simulated results: d) device 4; e) device 5 and f) device 6.

We then measured the EL emission spectra of these six OLED devices at different viewing angles, from normal direction to  $80^\circ$ . Results are plotted in Figs. 1(a-c) (weak cavity) and Figs. 2(a-c) (strong cavity), respectively. From Fig. 1, the weak microcavity OLEDs show a relatively broad spectral bandwidth, but the color shift at large viewing angles is not obvious. While for the strong microcavity OLEDs shown in Fig. 2, their EL spectra are much narrower than those of weak microcavity OLEDs, and a clear blue shift is observed for devices 4, 5 and 6. Accurate simulations were then performed, based on the theoretical model described above. The wavelength-dependent complex refractive indices of the OLED layers were measured by ellipsometry, and then used in our simulations. The simulated results are presented in Figs. 1(d-f) and Figs. 2(d-f). Excellent agreement between experiment and simulation is achieved, no matter for weak microcavity [Fig. 1] or strong microcavity OLEDs [Fig. 2].

As discussed above, both angular distribution mismatch and microcavity resonance effect contribute to angular color shift. Figure 3 plots the angular distributions of the emitted intensity for the six OLED samples. Simulations and measurements are also compared in order to validate our simulation model. Excellent agreement is again obtained as Fig. 3 depicts.

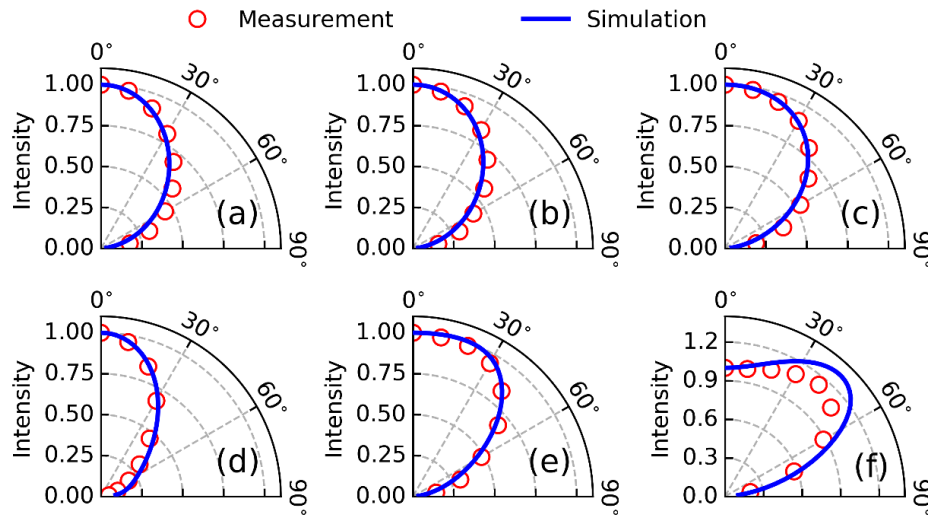


Fig. 3. OLED EL emission intensity angular distributions: a) device 1; b) device 2; c) device 3; d) device 4; e) device 5; and f) device 6.

To evaluate color shift quantitatively, we then calculated the CIE coordinate values. In this task, all the colors are described in CIE1976 color space instead of CIE1931 color space, because CIE1976 is more perceptually uniform and more suitable for color difference evaluation [22, 23]. The calculated CIE coordinate values of the six OLED samples are shown in Fig. 4. The three weak-microcavity OLED samples exhibit a much weaker angular color shift [Figs. 4(a-c)] than the strong microcavity ones [Figs. 4(d-f)]. The good agreement shown in Fig. 4 indicate that our simulation model can provide an accurate prediction on the angular color shift, of any OLED device, in spite of its microcavity strengths and resonance lengths. In summary, the proof-of-concept experiments have successfully validated our simulation model, from aspects of angular distribution [Fig. 3] and angular color shift [Fig. 4]. The optical behaviors of RGB OLEDs, including monochromatic color shifts and angular emission distributions, are actually determined by the same working mechanism, namely optical microcavity effect. That is the reason why we can extend our verified simulation method to red and blue OLEDs. To further analyze the second-type color shift induced by subpixels' angular distribution mismatch, we can first separately simulate the emission angular patterns of RGB OLEDs and then calculate the color shifts of the mixed colors by RGB color mixing.

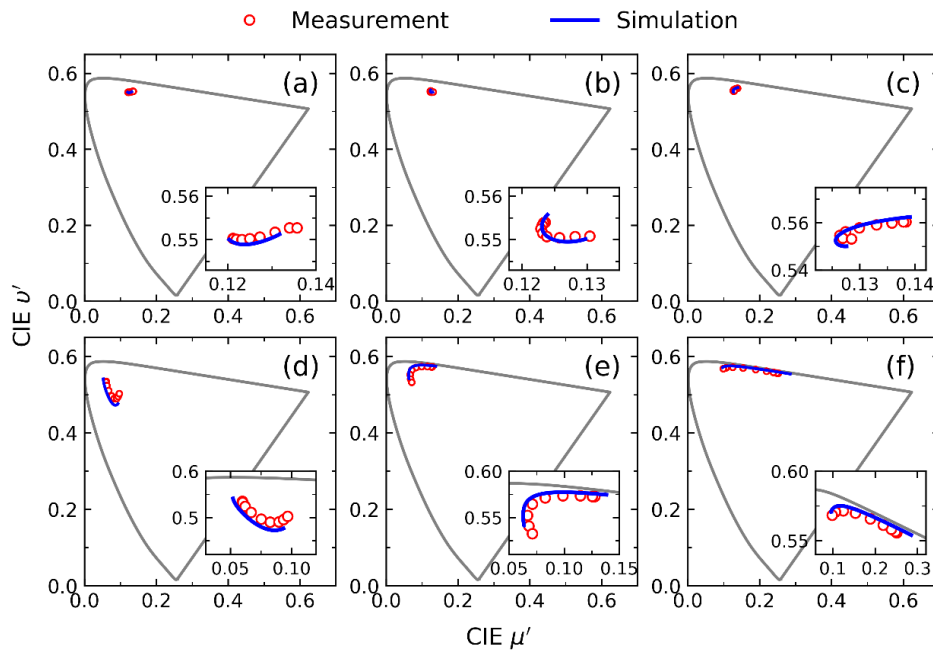


Fig. 4. Measured and simulated color shifts of OLED devices: a) device 1; b) device 2; c) device 3; d) device 4; e) device 5; and f) device 6.

#### 4. Systematic optimization

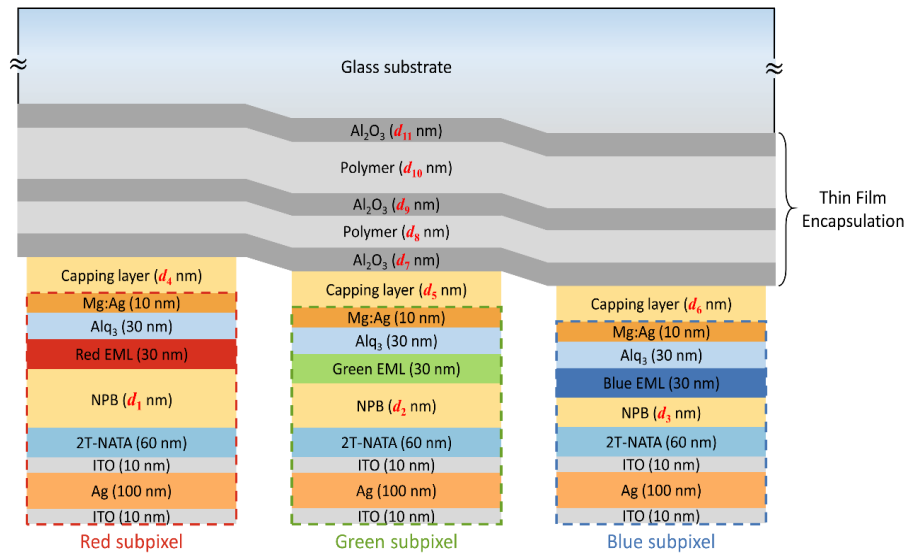


Fig. 5. Layer structures of OLED display system with Red, Green and Blue sub-pixels.

Based on the validated simulation model, we are able to perform systematic optimization for RGB-OLED displays. In the following simulations, the layer structure of the OLED display system is illustrated in Fig. 5. Each pixel in the OLED display consists of RGB subpixels. Mature device architectures of the RGB OLEDs are adopted, which are proven feasible for industrial production [24]. In all three subpixels, we used a bi-layer Ag/ITO as the reflective anode, 4,4',4''-Tris(N-(naphthalen-2-yl)-N-phenyl-amino)triphenylamin (2T-NATA) as the

HIL layer [24, 25], NPB as the HTL layer, Alq<sub>3</sub> as the ETL layer, and thin Mg:Ag alloy (10:1) as the semi-transparent cathode [24]. The bis(2-methyl-8-quinolinolato)(*para*-phenylphenolato) aluminium (III) (BAIq) doped with 10 wt% phosphorescent emitter bis(1-phenylisoquinoline)(acetylanetonate) iridium (III) (Ir(piq)<sub>2</sub>(acac)) [24] is adopted as the red emissive layer (Red-EML). The green EML is 8 wt% fac-tris(2-phenylpyridine) iridium (Ir(ppy)<sub>3</sub>) doped 4,4'-N,N'-dicarbazole-biphenyl (CBP) [26]. Due to operation lifetime concern, the blue subpixels utilize fluorescent blue emitter 1,4-di-[4-(*N*, *N*-diphenyl)amino]styrylbenzene (DSA-Ph), which is doped in host material 2-methyl-9,10-di(2-naphthyl)anthracene (MADN) with 5 wt% concentration [24]. The PL spectra of Red/Green/Blue materials in our simulations are extracted from previous publications [27–29]. The wavelength-dependent refractive indices of the organic layers are either obtained from ellipsometry measurement or extracted from literatures [30, 31].

As illustrated in Fig. 5, there is a thin dielectric capping layer (CPL) above the semi-transparent cathode. Such a capping layer has been found to significantly enhance the optical efficiency of OLED [32–34] by changing the microcavity effect. Actually, CPL has been widely used in practical OLED display devices. In our simulations, organic material NPB is used as the capping layer. One may also notice that the multilayered thin film encapsulation (TFE) is also included in the system architecture. Since OLED devices are extremely sensitive to moisture and oxygen, reliable encapsulation techniques are essential for commercial applications. The well-known BARIX multilayer technology [35] proposed by Vitex Inc, which involves organic-inorganic alternating stacks, can be very efficient to protect devices from the corrosion of water vapor and oxygen permeation. Recently, the atomic layer deposition (ALD) technique was applied to OLED encapsulation for preparing highly dense and much thinner barrier layer [36–38]. The employment of multilayered TFE would also affect the OLED emission performance [39, 40], due to optical interference. Thus for accurate optical analysis, the TFE multilayer should be taken into consideration as well. As shown in Fig. 5, our TFE consists of five Al<sub>2</sub>O<sub>3</sub>/Polyacrylate alternating layers. The input parameters to be optimized are the thicknesses of the HTL, CPL and TFE layers. In total, there are eleven independent variables in our optimization, which can be denoted by  $D = [d_1, d_2, d_3, \dots, d_{11}]$ . The parameter boundary constraints actually depend on the practical requirements. In particular, the HTL layer thickness is set to be less than 250 nm to avoid electrical property distortion. In order to maintain reliable barrier performance, Al<sub>2</sub>O<sub>3</sub> layers are kept thicker than 5 nm during optimization.

As mentioned above, three metrics need to be considered to evaluate the RGB OLED display performance. The first one is the optical out-coupling efficiency. As to three subpixels, their optical efficiencies are denoted as  $EQE_R$ ,  $EQE_G$  and  $EQE_B$ , respectively. The first optimization objective can be defined as the arithmetic average, weighted average or minimum value of  $EQE_R$ ,  $EQE_G$  and  $EQE_B$ , according to the specific application needs. In this work, the minimum value  $EQE_{\min} = \min\{EQE_R, EQE_G, EQE_B\}$  is adopted as the first objective. In terms of color behaviors, wide color gamut and weak angular color shift are preferred. In the color gamut evaluation, there actually exist several different definitions. We use the color gamut coverage ( $CGC$ ) in the normal viewing direction as the second objective, which can be expressed as:

$$CGC = \frac{A_{display} \cap A_{standard}}{A_{standard}}, \quad (3)$$

where  $A_{display}$  stands for RGB triangular area of the display and  $A_{standard}$  is the triangular area of the reference standard. In our simulation, the wide color gamut DCI-P3 with D65 white point is used as the standard, as illustrated in Fig. 6. The third metric is the angular color shift. In order to evaluate the color shift throughout the entire color gamut, we have defined 10 reference colors in total. These reference colors include three primary colors, white point

D65, and six mixed colors. With DCI-P3 primary colors as an example, 10 reference colors are plotted in CIE1976 color space [Fig. 6]. The optimization objective is defined as the maximum value of the average color shift  $\Delta\mu'v'_{\max}$  of 10 reference colors from  $0^\circ$  to  $60^\circ$  viewing angle.

The systematic optimization of an RGB OLED display involves 11 input parameters and 3 objectives. Such a multi-parameter and multi-objective optimization would generally consume massive computational resource and long computational time. To speed up the simulation program, multicore parallel computing technique has been adopted. In our workstation with two 14-core Intel Xeon E5-2660 processors, the execution time of one performance evaluation of an RGB OLED display is shorter than 0.25 seconds. Such a fast computation time enables numerous iterations for optimization. To ensure that the global optimal solutions can be determined, four optimization algorithms, Genetic Algorithm (GA), Adaptive Simulated Annealing (ASA), Particle Swarm Optimization (PSO) and Differential Evolution (DE), have been interchangeably used during the optimization. As for a multi-objective optimization problem, any further improvement of the solution in terms of one objective is likely to be compromised by the degradation of another objective. Such optimal solutions constitute a *Pareto Front* [41]. In our optimization for the above-mentioned RGB OLED system, more than 1,000,000 iterations have been implemented to give 2,000 optimal solutions. All the optimal solutions visualize the *Pareto Front* of this 3-objective optimization, as illustrated in Fig. 7.

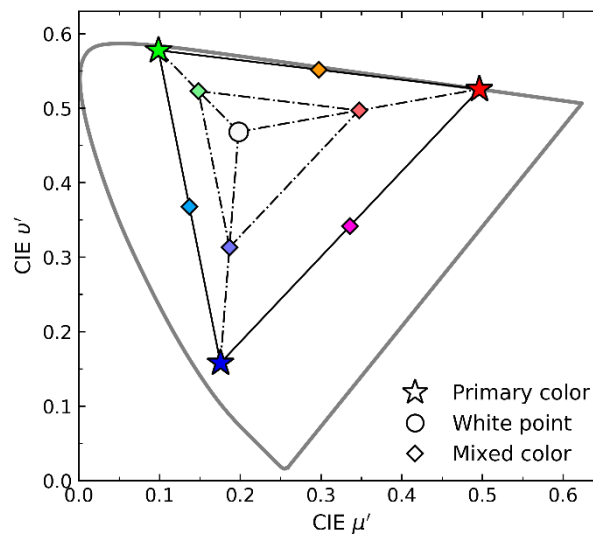


Fig. 6. 10 reference colors in CIE1976 color space, with DCI-P3 primary colors and D65 white point.

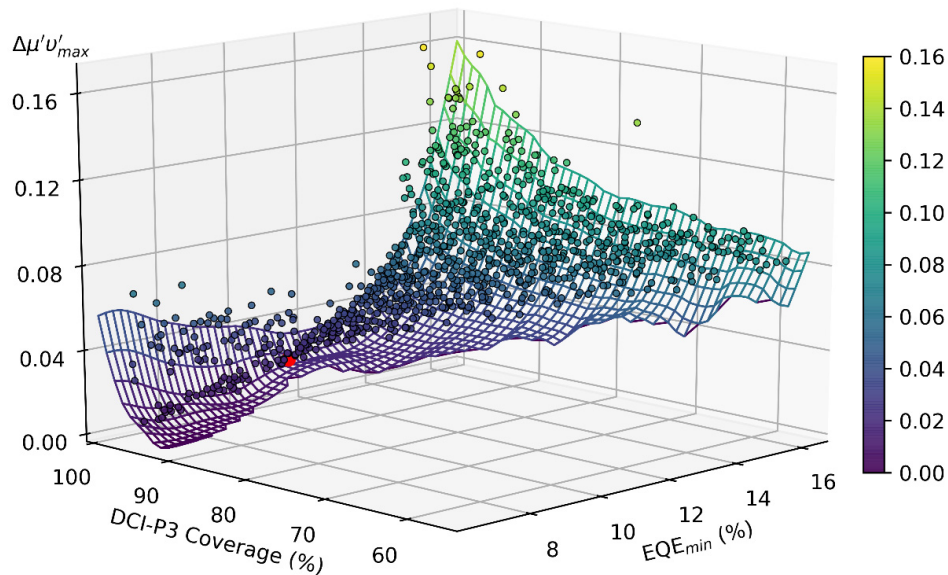


Fig. 7. The *Pareto Front* of the 3-objective systematic optimization for the RGB OLED display system. (Red dot: optimal solution 1)

## 5. Results

Each point on the *Pareto Front* surface in Fig. 7 presents an optimal solution. It describes the weakest color shift  $\Delta\mu'\nu'_{\max}$  we can obtain without sacrificing *EQE* and color gamut. The *Pareto Front* surface geometry reveals the intrinsic trade-offs between optical efficiency, color purity and angular color shift. As the microcavity effect gets stronger, the *EQE* and color gamut coverage increase, but the angular color shift worsens, as Fig. 7 shows. Appropriate optimal solutions can be selected according to different application needs. Here we choose one example: optimal solution 1 (Op1) in Fig. 7, for detailed analysis. The OLED layer thicknesses for optimal solution 1 are  $D = [184 \text{ nm}, 114 \text{ nm}, 69 \text{ nm}, 39 \text{ nm}, 174 \text{ nm}, 116 \text{ nm}, 56 \text{ nm}, 107 \text{ nm}, 77 \text{ nm}, 126 \text{ nm}, 112 \text{ nm}]$ . As for this system architecture, the optical efficiencies of the RGB OLEDs are  $EQE_R = 11.3\%$ ,  $EQE_G = 17.5\%$ , and  $EQE_B = 13.7\%$ . The average efficiency is  $EQE_{\text{ave}} = 14.2\%$ . In comparison with commercialized planar RGB OLED system whose optical efficiency is normally  $\sim 20\%$ , the Op1 system can achieve 71% optical efficiency *EQE* of the commercial one. Another significant advantage of top-emitting OLED is its excellent color purity. Thus, we also need to examine the color performance of Op1 OLED display. The color triangle of Op1 is plotted in CIE1976 color space, as shown in Fig. 8. The optimized OLED display Op1 can cover 99.02% of DCI-P3 standard and 88.26% of Rec. 2020 standard. In terms of triangular area ratio, its area can achieve 121.12% of the DCI-P3 triangular area. The optimized OLED device presents an excellent color performance.

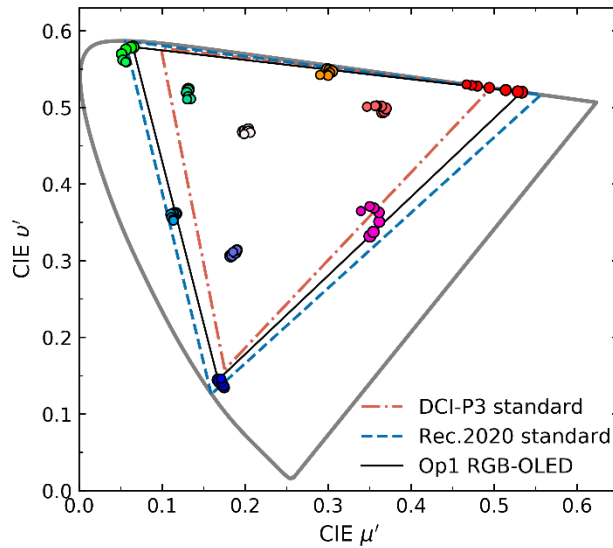


Fig. 8. Simulated color triangle of the Op1 RGB OLED display system and the angular color shifts of 10 reference colors from 0° to 60° viewing angle.

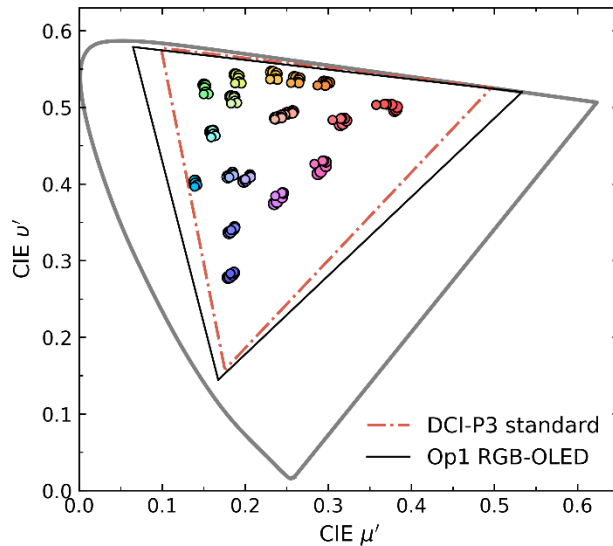


Fig. 9. Simulated angular color shifts of the first 18 colors in Macbeth ColorChecker from 0° to 60° viewing angle.

Next, we investigate the angular color shift. Figure 8 depicts the CIE coordinates of 10 reference colors at different viewing angles, from 0° to 60° with 10° interval. The average color shift  $\Delta\mu'v'$  at 60° is only 0.019, which is good enough for commercial applications. As Fig. 8 indicates, the red channel has the most severe angular color shift. It is harder for red subpixels to get high efficiency, pure colors and weak color shift simultaneously than green and blue subpixels. This is the bottleneck for the RGB OLED display system optimization. One thing noteworthy is that some colors are actually more important than the others in a display system. The Macbeth ColorChecker [42] is commonly used as the reference in color tests and reproductions. It is designed to mimic the colors of natural objects such as human skin, foliage, and flowers. We also evaluate the color shifts of the first 18 colors from

Macbeth ColorChecker based on our Op1 RGB OLED system. The angular color shifts are illustrated in Fig. 9. The color shifts of all 18 colors within  $60^\circ$  viewing cone are kept below 0.02 and the maximum value of average  $\Delta\mu'v'$  from  $0^\circ$  to  $60^\circ$  is only 0.0102, which is visually indistinguishable.

## 6. Discussion

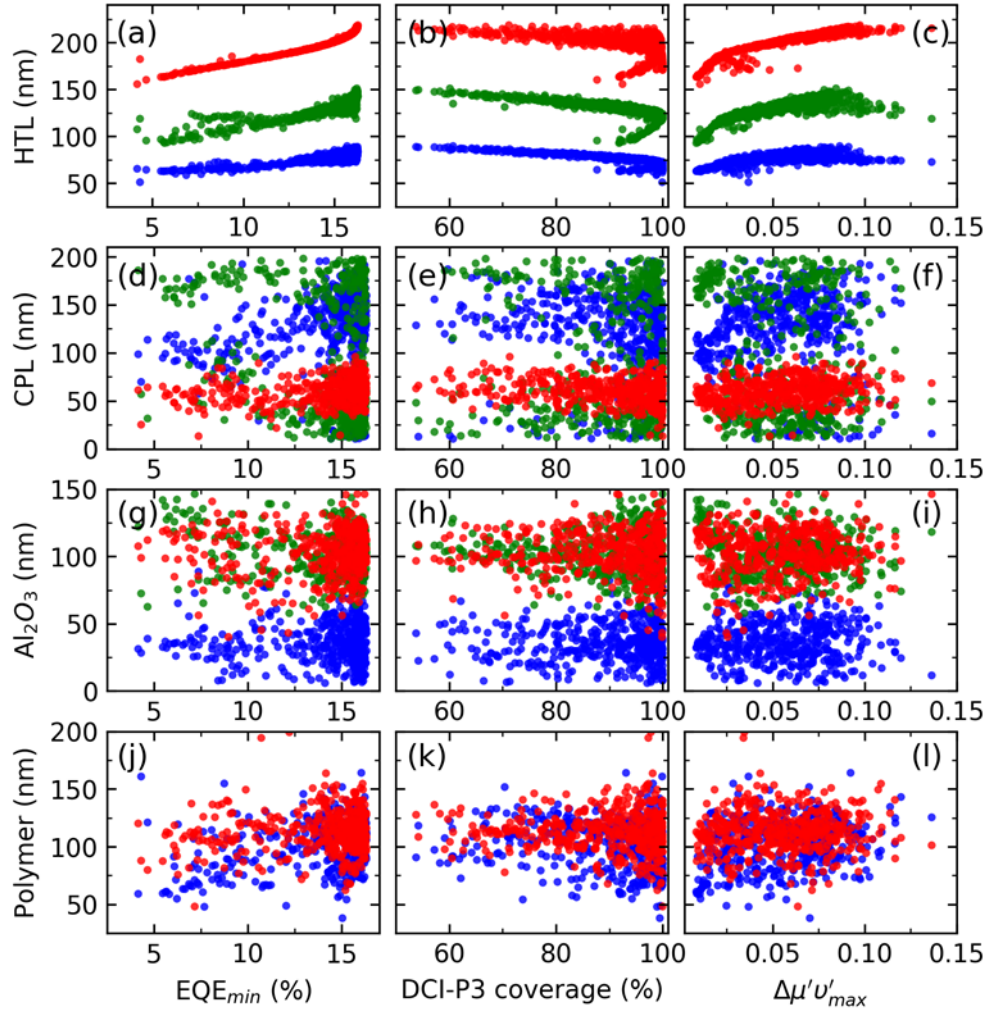


Fig. 10. The correlations between the OLED optical behaviors and the layers' thickness: (a)(b)(c) HTL layers (red- $d_1$ , green- $d_2$ , blue- $d_3$ ); (d)(e)(f) CPL layers (red- $d_4$ , green- $d_5$ , blue- $d_6$ ); (g)(h)(i) Al<sub>2</sub>O<sub>3</sub> layers in thin film encapsulation (blue- $d_7$ , green- $d_8$ , red- $d_{11}$ ); (j)(k)(l) polymer layers in thin film encapsulation (blue- $d_8$ , red- $d_{10}$ ).

In the above section, we have discussed the optimal solutions obtained by multi-objective optimization algorithm. In addition to optimization results, we may still need to examine the relationships between the emission behaviors and the thickness of each layer. In Fig. 10, for each of the 2000 optimized configurations, we plot the thickness of HTL [Figs. 10(a-c)], capping layers [Figs. 10(d-f)] and thin film encapsulation layers [Figs. 10(g-l)] with their corresponding optical performances. Figure 10 clearly illustrates that the HTL layers have higher impact on optical behaviors than other layers. The systematic optimization applies stricter constraint on HTL's thickness. For instance, if a high EQE<sub>min</sub>~15% is achieved, the HTL

thickness of red OLED needs to be  $200 \pm 5$  nm [Fig. 10(a)], while the capping layer can be in the range of 40 ~90 nm [Fig. 10(d)]. Thus, the optical performances are more sensitive to the thickness of HTL layers. Actually, such a phenomenon is in accord with our expectation, since the HTL layer is located between two metal electrodes and it can directly affect the cavity length of OLEDs. As for CPL and encapsulation layers, our proposed systematic optimization algorithm has also provided the optimal thickness ranges for these layers. Within the optimal range, the device performances are not very sensitive to the layer thickness.

## 7. Conclusion

We have analyzed the angular color shift issue and proposed a systematic multi-objective optimization method for planar RGB-OLED displays. First, we experimentally validate our simulation model for both strong and weak cavity OLEDs. With utilizing four optimization algorithms, external quantum efficiency (EQE), color gamut coverage, and angular color shift can be optimized simultaneously. The obtained optimization *Pareto Front* not only reveals the intrinsic trade-offs between efficiency, color gamut, and color shift, but also provides valuable guidelines for improving the RGB OLED display system. The optimized RGB OLED display system shows indistinguishable angular color shifts, wide color gamut, and relatively high optical efficiency.

## Funding

Industrial Technology Research Institute (ITRI), Taiwan.